Kwon *et al.*
Journal of Analytical Science and Technology (2023) 14:37
https://doi.org/10.1186/s40543-023-00402-4

Journal of Analytical Science and Technology

TECHNICAL NOTE

Open Access

Effective investigation of murine femoral bone development utilizing correlative light and electron microscopy (CLEM)

Yong-Eun Kwon[1†], Jung-Kyun Kim[1,4†], Youn-Joong Kim[1], A. Reum Je[2], Hwanuk Guim[3*] and Jin-Gyu Kim[1*]

Abstract

Background For effective investigation of the developing structure and chemistry of bone, comprehensive studies including compositional analysis can be achieved through the gradual observation from the micro- to nanometer scale via correlative light and electron microscopy (CLEM). This technique is particularly useful considering the complex hierarchical arrangement of bioapatite and collagen fibrils which may vary according to specific bone tissue types (i.e., lamellar bone and woven bone) and different growth stages. Scanning electron microscopy (SEM) accompanied with the attachment of the scanning transmission electron microscopy (STEM) detector, referred to as the STEM-in-SEM can be utilized to produce high contrast images from materials composed of light elements, and efficiently allows the selection of suitable accelerating voltage for energy-dispersive spectroscopy (EDS). This study aims to emphasize the efficacy of CLEM techniques through applying STEM-in-SEM and EDS analyses, and its application to comparative murine bone investigation in differing ontogenetic stages.

Findings We have designed a new grid-holder which can be used for both light and electron microscopy, and we presented an imaging technique for TEM specimens via reflective light microscopy (RLM). For performing CLEM, ultra-thin-sections (UTS) prepared from the femoral bones of 1- to 16-week old of Sprague-Dawley (SD) rats provided light and electron micrographs that can be correlated based on the regions of interest (ROIs). STEM-in-SEM micrographs revealed information not attainable by secondary electron (SE) and back-scattered electron (BSE) micrographs. In addition, for analyzing chemical variation according to growth and development of femoral bones from 1- to 16-week-old rats, comparative chemical analysis was performed through STEM-in-SEM EDS with two reference materials.

Conclusion Herein, from femoral bones of SD rats, we have confirmed the rapid chemical and structural variations within the first 8 weeks after birth. STEM-in-SEM micrographs revealed the bone development process of the early stage porous bone matrix subsequently being filled with collagen fibrils and bioapatite. In addition, chemical analysis for carbon and oxygen showed the ratios of inorganic to organic phases according to growth and progress in bone mineralization. As a result, we were able to postulate the growth mechanism of murine femoral bone in the neonatal stages of development. We also anticipate that our CLEM techniques can be further utilized for more thorough investigation of bone structure and chemistry in diverse scales.

†Yong-Eun Kwon and Jung-Kyun Kim have contributed equally to this work.

*Correspondence:
Hwanuk Guim
huguim@kbsi.re.kr
Jin-Gyu Kim
jjintta@kbsi.re.kr
Full list of author information is available at the end of the article

Keywords Correlative light and electron microscopy (CLEM), STEM-in-SEM, Energy-dispersive spectroscopy (EDS), Multi-grid-holder, Ultra-thin section (UTS), Sprague-Dawley (SD) rat

Introduction

The mineral phase of bone is mainly composed of bioapatite, a biological derivative of hydroxyapatite ($Ca_5(PO_4)_3(OH)$), which is aligned along with collagen fibers. Although previous studies have reported that the CO_3 group can substitute either the PO_4 or OH sites within the apatite crystal structure, it is difficult to precisely measure the amount of C and O composing bioapatite due to the organic constituents of bone such as the aforementioned collagen fibers, bone-forming proteins, lipids, and other biomacromolecules (Wopenka & Pasteris 2005; LeGeros et al. 2009; Wang et al. 2010; Hughes 2015). Additionally, as the arrangement of bioapatite and collagen produces complex hierarchical structures leading to specific tissues such as woven or lamellar bone, comprehensive studies on bone including composition analysis usually require gradual observation from micro- to nanometer scales via correlative light and electron microscopy (CLEM) (Glimcher 2006; Takizawa and Robinson 2012; Burr and Allen 2013).

With the ongoing advances of detector technology for electron microscopy (EM), the scanning transmission electron microscopy (STEM) detector which is developed to collect transmitted electron signals is not only applied to transmission electron microscopy (TEM), but can also be utilized in scanning electron microscopy (SEM) (Probst et al. 2007; Guise et al. 2011; Beyer et al. 2012; Hondow et al. 2012; Holm & Keller 2016). As a SEM instrument equipped with a STEM detector (referred to as STEM-in-SEM) uses lower accelerating voltages; usually below 30 kV, it has the advantage of producing high contrast images for materials composed of light elements compared to TEM (Guise et al. 2011). In addition, since flexible changes in accelerating voltages are easily performed in STEM-in-SEM, it is suitable to find optimal analytical conditions for chemical analysis utilizing the energy-dispersive spectroscopy (EDS) system, based on the properties of the specific samples that are being investigated (Williams and Carter 2009; Wu et al. 2015; Kim et al. 2018; Goldstein et al. 2018).

This study proposes improved CLEM techniques applying STEM-in-SEM and EDS analyses on murine bone structure and chemistry investigation according to differing ontogenetic stages. In order to effectively apply STEM-in-SEM EDS analysis for bone investigation, we have designed a new CLEM holder and performed chemical analysis on the femoral bones from 1- to 16-week-old female Sprague-Dawley (SD) rats. The CLEM holder can simultaneously load up to nine TEM grids and is composed of thin upper and lower plates to reduce the fault (noise) signals generated from the holder itself. In addition, the holder is easily transferable to light microscopes and the loaded samples are effectively observable through reflective light microscopy (RLM). We have utilized ultra-thin-sections (UTS) prepared from the femoral bones of SD rats via an ultramicrotome, which allowed us to observe the transverse cross section of the sampled bones via CLEM including RLM and STEM-in-SEM. By utilizing STEM-in-SEM EDS analysis, we have carried out comparative chemical analysis on seven UTS specimens of SD rats with two reference materials, synthetic apatite ($(Ca_5(PO_4)_3(OH))$ and precipitated calcium carbonate ($CaCO_3$), all within the same analytical conditions (Kwon et al. 2019). In order to interpret the changes of inorganic (Ca, P and O) and organic (C and O) elements according to the ages of the SD rats, we have particularly focused on carbon analysis with consideration of potential carbon sources that may originate from the analytical environment.

As a result, STEM-in-SEM micrographs and EDS analysis data reveal the possibility that collagen fibrils and bioapatite subsequently fill the pores of the bone matrix around the osteocyte lacunae, and such ossification processes in early growth stages have not been clearly presented from previously reported techniques (Shah et al. 2019).

Experimental methods

Ethics statement

Animal studies were performed after obtaining approval from the Institutional Animal Care and Use Committee in the Korea Basic Science Institute (KBSI-ACE1013).

Sample preparation

1- to 16-week-old female SD rats were obtained from Daehan Biolink (DBL) Co., Ltd, South Korea. The femoral bones were prepared through dissection soon after the rats were euthanized, which underwent dehydration in 70% ethanol solution for 24 h in room temperature. A critical point dryer (Samdri-PVT-3D, Tousimis) was used to thoroughly dry the femoral bones for approximately 1 h prior to sectioning.

Dried femoral bones were fabricated as LM specimens, bone blocks, and UTS specimens as shown in Fig. 1 for CLEM investigation (Kwon 2020). A diamond wire saw (Precision diamond wire saw 3242, Well) with a wire

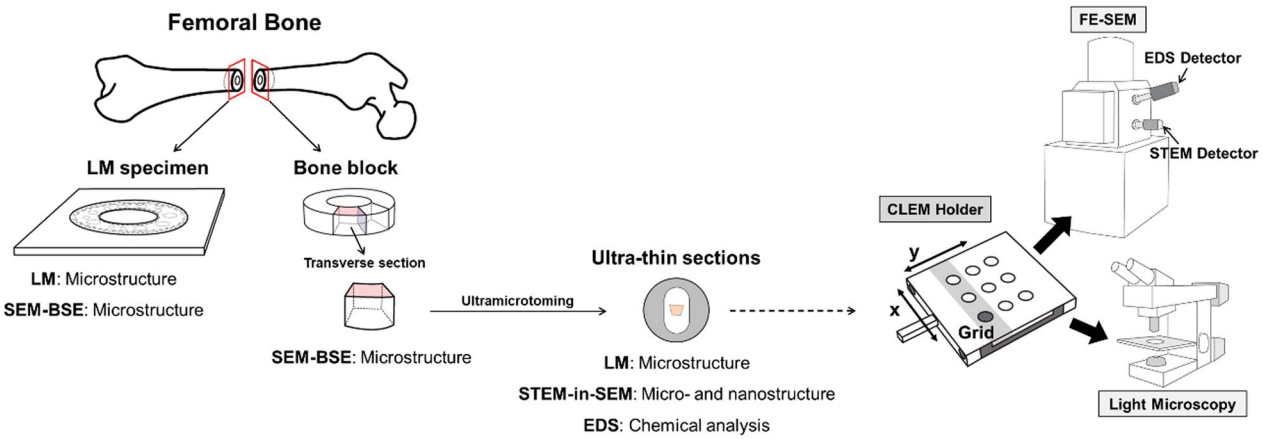

Fig. 1 Preparation of femoral bone for CLEM investigation and utilization of the CLEM holder for various instruments. In order to maintain the correlative aspects of CLEM, observation sections from the regions of interest (ROIs) of LM specimens, bone blocks, and UTS specimens were carefully prepared and were analyzed via each instrument from LM to EM. The CLEM holder is capable of loading nine UTS specimens and is applicable to a variety of SEM instruments with STEM and EDS detectors installed. The holder loaded with TEM specimens is easily transferable for LM which is analyzed using either transmitted or reflected light, which enhances the efficacy of CLEM. (EM: Electron microscopy. LM: Light microscopy. UTS: Ultra-thin sections)

thickness of 120 μm was used to obtain approximately 500 × 500 × 500 μm sized blocks for ultra-thin sectioning from the mid-diaphyseal region. The bone blocks were embedded in epoxy resin (Embed-812 kit, EMS) which was mixed with the following composition—EMbed-812 20 ml, DDSA 16 ml, NMA 8 ml, and DMP-30 0.88 ml. The prepared resin solution was further mixed by vortexing (Vortex Seoulin Bioscience), and underwent centrifugation (CF-10, Daihan Scientific) around 10 s at 13,500 rpm to remove visible air bubbles. The resin solution was poured into a mold (Flat embedding mold blue, Pelco), and the bone blocks were carefully placed in the mold under observation through a stereoscopic zoom microscope (SMZ 1500, Nikon) for subsequent slicing of the transverse plane. A temperature-humidity controller (TH-PE, JEIO Tech) set to 60 °C was used to harden the embedding resin for 24 h without any adjustments in the humidity level. The hardened resin blocks were sectioned via an ultramicrotome (Ultracut UCT, Leica) with a targeted thickness of 100 nm for every serial section. The prepared sections were then loaded on TEM grids (2 × 1 mm slot ultrathin-carbon film grids, EMS).

Synthetic apatite (hydroxyapatite, $Ca_5(PO_4)_3(OH)$, 574791-15G, 99.999%, Sigma-Aldrich) and precipitated calcium carbonate nanoparticles (calcium carbonate, $CaCO_3$, US3701, 50 nm, 98%, US Research Nanomaterials, Inc) were used as reference materials, which were available in powdered form and were added into 99.9% ethanol solutions. After dispersing the nanoparticles by a probe sonicator (EpiShear, Active Motif), each sample solution was sprayed onto an individual TEM grid (2 × 1 mm slot ultrathin-carbon film grids, EMS) using a custom-developed ultrasonic sprayer to prevent aggregation of particles as well as to adequately disperse the sample particles widely enough to facilitate drying of the solution on the TEM grid (Kim et al. 2018).

Development of the grid-holder for CLEM

Although there are a variety of manufactured TEM grid-holders for SEM instruments, we have previously developed a multi-grid-holder suitable for EDS analysis in a table-top SEM designed to minimize EDS noise signals from the holder itself (Kwon et al. 2019). In this study, a new multi-grid-holder called as the 'CLEM holder' has been designed to broaden its utilization for CLEM of biological samples, which is capable of loading nine TEM grids and can be used to reliably perform EDS analysis as shown in Fig. 1. In addition, the holder can be used for LM to view the samples either through transmitted or reflected light (Fig. 1).

The holder is easily transferrable to LM utilizing the LM adapter, as shown in Fig. 2A and B, for performing effective CLEM analysis which is essential for investigating biological samples. Before carrying out STEM-in-SEM imaging and EDS analyses, prior observation of the UTS specimens through LM is mandatory to select the ROIs. In the case of UTS specimens as shown in Fig. 2A, RLM effectively expressed the interference color by path differences occurring from the thin specimen, which resulted in micrographs with higher contrasts compared to other LM imaging techniques such as phase-contrast microscopy (Kwon 2020). In addition, the extremely thin thickness of UTS specimens minimized the image overlap effect that generally occurs from thicker sections

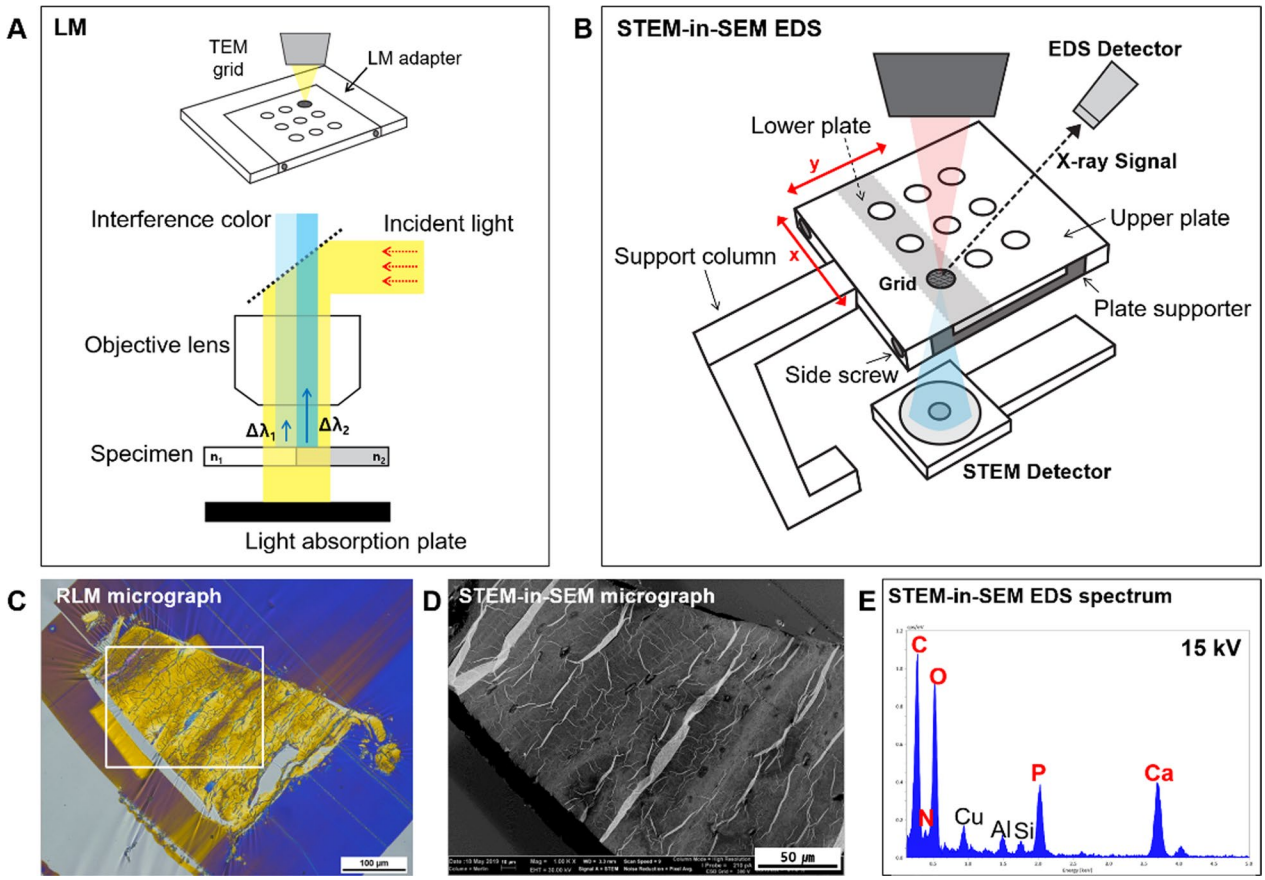

Fig. 2 Application of the CLEM holder for bone study. **A** Schematics of the CLEM holder applied for LM observation. In the case of the UTS specimen, RLM is effective due to interference colors providing high contrast by reflective light. In addition, the light absorption plate was used together to avoid light reflecting back after passing through the specimen. **B** The configuration for STEM-in-SEM EDS using the CLEM holder and its components. **C** A RLM micrograph of a femoral transverse section from an 8-week-old rat. **D** A STEM-in-SEM micrograph obtained at the location shown in the marked region of (C). **E** An EDS spectrum acquired from the bone matrix of (D). The spectrum shows Ca, P, C, and O as the main composing elements of bone. The weak Cu, Al, and Si signals are generated from the TEM grid, holder, and STEM detector, respectively. (EDS: Energy-dispersive spectroscopy. LM: Light microscopy. RLM: Reflected light microscopy. STEM-in-SEM: Scanning transmission electron microscopy-in-scanning electron microscopy. UTS: Ultra-thin sections)

typically used in biological LM, which allowed us to obtain higher resolution images (Takizawa and Robinson 2012).

The holder is composed of an upper plate, a lower plate, plate supporters, side screws, and a support column as shown in Fig. 2B. The upper plate and lower plate were fabricated to be as thin as possible to direct sample EDS signals into the detector, which also allows observation in shorter working distances at higher magnifications for both SEM and LM. Because the thin plates themselves were insufficient to firmly hold TEM grids, the plates were fixed using the plate supporters and side screws. The newly applied assembly of the holder mitigated the limitations of the previous holder which was only capable of loading four grids due to the bulky lower support part (Kwon et al. 2019). Furthermore, with the increased holder capability up to nine TEM grids, the new holder was much more efficient to investigate multiple biological samples under consistent analytical conditions. In the case of the commercial STEM holder for the FE-SEM instrument utilized in this study, the holder is designed to rotate the sample loading part like a carousel to view and analyze different samples, and due to its unique design, it is not compatible with other SEM instruments (Guise et al. 2011). However, the new holder is assembled to have the support column facing outwards to minimize the generation of fault (noise) signals as shown in Fig. 2B.

To perform chemical investigation on bone, we loaded nine UTS specimens prepared from seven SD rats at different growth stages along with two reference materials on the holder. Before carrying out STEM-in-SEM EDS analysis, we observed the UTS specimens through LM. The RLM micrograph in Fig. 2C displays a femoral transverse section from the 8-week-old SD rat. Since

the expressed interference colors represent the refractive indices, we expect that RLM can provide additional information related to bone mineral density. Figure 2D and E illustrates the CLEM process applied to this study, which involves transferring the CLEM holder for STEM-in-SEM analysis right after RLM observation, and obtaining STEM micrographs and EDS spectra from the marked ROIs (white box) in Fig. 2C.

STEM-in-SEM EDS analysis

Given the larger chamber space, STEM-in-SEM allows the loading of higher number of samples compared to TEM, enabling simultaneous analysis alongside standard samples for direct comparison. Moreover, it provides high-contrast imaging for samples with low-density or low atomic number, allowing clear visualization of such samples at high resolution. The wide field of view enables gradual observations at various magnifications, ranging from micro- to nanostructures. STEM-in-SEM, which uses a lower voltage than that of TEM, may also have lower specimen penetration levels, but it was shown to be adequate of acquiring images for 100-nm-thick specimen in bio-samples. In chemical analysis, STEM-in-SEM excels with the flexibility of voltage selection below 30 kV, which is particularly advantageous for EDS analysis. This capability facilitates more thorough analysis of light elements, making it highly versatile in a range of applications. Thus, such advantages of STEM-in-SEM EDS can be applied to bone analysis.

Because bone is composed with both organic and inorganic phases, our comparative chemical analysis method contemplates selecting the suitable accelerating voltage for organic–inorganic complexes using the Monte Carlo simulation with the software CASINO 2.51 (Mendis 2018; Hodoroaba et al. 2019; Kwon 2020). For major bone constituting elements (Ca, P, C, N, and O), they have a wide range (0.282 ~ 3.391 keV) of their ionization energy from carbon ($Z=6$) to calcium ($Z=20$). In addition, since the X-ray signal of each element is generated from collagen or/and apatite, it is difficult to determine values by brief calculations based on the ionization yield.

Considering the interaction volumes inside collagen and apatite in 100 nm thickness at 5 kV, 15 kV, and 30 kV by the Monte Carlo simulations, a previous study mentioned that X-ray generation inside the thin specimen may not be consistent by the degree of mineralization and/or bone development because the interaction volumes of collagen and apatite in 5 kV-simulation has the largest difference (Kwon 2020). In addition, a previous study indicated that the effect from thickness for X-ray generation of all elements (Ca, P, C, N, and O) at high accelerating voltage was reduced, but the X-ray generation of light elements became low (Kwon 2020). As simulation results may vary under different conditions, it has been reported that the X-ray generation from collagen and apatite at 5 kV was not constant depending on the thickness of specimens (Kwon 2020). The detection of carbon can be advantageous when a low voltage is used, but we have also aimed to simultaneously analyze inorganic elements (Ca and P) and organic elements (C, N and O) in each session. In addition, it is difficult to obtain consistent data because the electron interaction volume may vary depending on the degree of mineralization and thickness of the samples. We would also like to emphasize that our analytical conditions are aimed at the aforementioned simultaneous analysis of organic and inorganic elements, rather than solely focusing on light elements. To conduct chemical analysis on bio-samples, the selection of analytical conditions may vary depending on the constituent elements and analysis purposes. We have emphasized the considerations for determining these conditions, including factors such as the electron interaction volume inside samples and the accelerating voltage for ionization. Furthermore, to ensure the reliability of our analyses, obtaining data from statistically significant locations is of paramount importance.

In this study, considering the results of the Monte Carlo simulation, we strongly recommend STEM-in-SEM EDS for chemical investigation of bone because selecting the suitable accelerating voltage for analyzing the collagen–apatite complex is feasible.

After the CLEM holder loaded with UTS specimens and reference materials was observed by RLM (Eclipse 80i, Nikon; mercury light source), it was transferred into a FE-SEM (Merlin, Carl Zeiss) operating at 0.02–30 kV equipped with an EDS detector (XFlash 6160, Bruker; take-off angle: 35°). Seven UTS specimens and two reference materials were analyzed under the same analytical condition for each session. Initially, STEM-in-SEM dark-field micrographs were obtained via a STEM detector (Carl Zeiss) at 30 kV. EDS analysis was subsequently conducted on the bone matrices, and 20 spectra per specimen were collected at 15 kV. Each spectrum was collected for 100 s from the 1 × 1 μm area. Additionally, in order to identify background signals, 20 spectra from the carbon film of the TEM grids were also collected. Analysis and data processing of all spectra were done with the Bruker software Esprit 2.0.0. As the EDS analysis time increases, hydrocarbons continue to accumulate on the sample surface, leading to a continuous increase in the carbon background signal in the EDS spectrum. This can result in a relative decrease in the carbon signal of the sample, making it unreliable to estimate the actual amount of carbon in the specimen. When analyzing the amount of carbon using EDS analysis, it is crucial to identify the source of background carbon signals. In our

study, we identified the sources of carbon as hydrocarbons accumulated on the surface due to electron beam irradiation and the carbon film supporting the sample section. To determine the amount of background carbon, we obtained spectra under the same conditions from the carbon film.

The counts as the integrated intensity of the peak for each element extracted from all spectra was used for comparing the change of elements in the SD rats. Figure 3 presents spectra obtained from the two reference materials at 15 kV, which were applied for comparing with the acquired spectra from the SD rats; Ca and P counts were compared with the synthetic apatite data, and C and O counts were compared with the precipitated calcium carbonate data.

Results and discussion

CLEM for SD rat femoral bones

In order to investigate the femoral bones from 1- to 16-week-old SD rats, we have measured the long axis lengths and transverse cross-sectional areas based on femoral micrographs, and the measured values were expressed in the graph shown in Fig. 4. The graph suggests that femoral bones have grown rapidly between 1- to 8-weeks of age, and undergone extensive bone remodeling, especially in transverse volume (Burr and Allen 2013, Piemontese et al. 2017). We have performed CLEM analysis for specimens prepared as shown in Fig. 1. Figure 5 displays various micrographs obtained from each specimen via specific instruments for CLEM, which is organized by rows (A ~ D) representing the age of the rats and columns (1 ~ 4) representing imaging techniques.

Light micrographs in Fig. 5 (column 1) confirm that femoral bone becomes denser and differentiation of bone tissue occurs according to aging. Especially, in the case of the 1-week-old rat, it was observed that

Table 1 Analytical conditions for acquiring EDS spectra of reference samples (SAp and PCC) in Fig. 3

EDS analysis conditions	
Accelerating voltage	15 kV
Probe current	< 200 nA
Specimen thickness	100 nm (approximately)
Specimen tilt	0 °
Acquisition area size	1 um × 1 um (Area acquisition mode)
Acquisition time	100 s
Number of spectrum acquisitions	20 times
Take-off angle of the EDS detector	35 °
Detector active area	60 mm^2

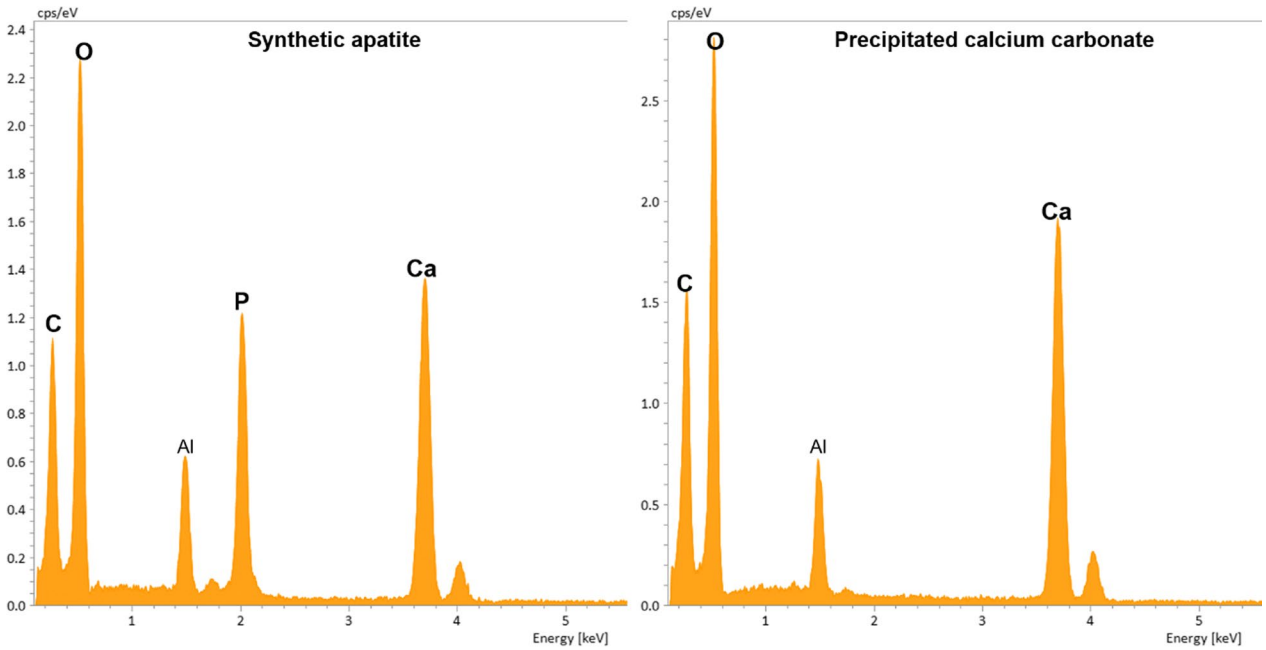

Fig. 3 EDS spectra from the reference materials (synthetic apatite and precipitated calcium carbonate). EDS spectra obtained from the reference materials (synthetic apatite and precipitated calcium carbonate) at 15 kV, in order to compare the ratios of elements in bone samples. Refer to Table 1 for context on analytical conditions, and the 'Experimental Methods' section for details on the reference materials.

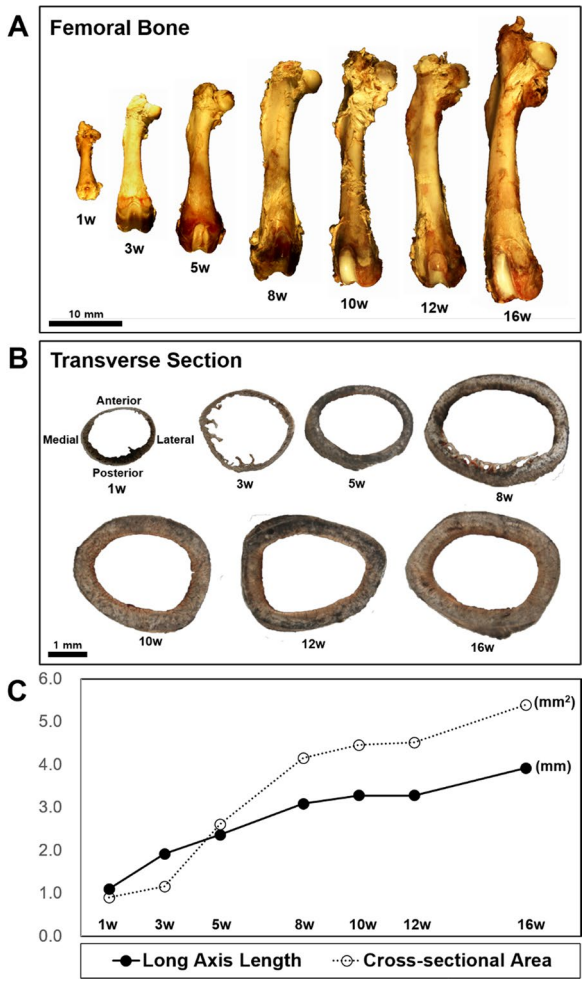

Fig. 4 Comparative micrographs of femoral bones from 1- to 16-week-old SD rats, and the measurements of long axis length and cross-sectional area. **A** Micrographs of dissected femoral bones before preparation. **B** Micrographs of transverse cross-sections from the femoral bones. **C** Representative graph of long axis length and cross-sectional area measurements from (**A**) and (**B**)

mineralization of the bone matrix has hardly progressed. Although BSE micrographs obtained from the bone blocks provided distinct structural features such as canaliculi, osteocyte lacunae, and calcified cartilage distributed throughout bone matrix, it was insufficient to discern the degree of mineralization. As shown in the BSE micrographs in Fig. 5 (column 2), the bone matrix of a 1-week-old rat (Fig. 5A2) is highly porous, and the density increases around 3 weeks in age. In addition, other noticeable structural features such as osteons and osteocyte lacunae are unclear in the matrices of 1- and 3-week-old rats, but becomes distinguishable in the bone matrix of 5- and 8-week-old rats.

In this study, to improve CLEM utilization for bone investigation, the application of biological UTS specimens was particularly effective with the CLEM holder. Before performing STEM-in-SEM analysis on UTS specimens, RLM was specifically applied for selecting ROIs on specimens and also for evaluating the specimen state in order to proceed the steps more efficiently. In addition, RLM gave us high contrast images which can be used as a proxy to determine the degree of bone mineralization. The bone matrix of the 1-week-old rat shown in Fig. 5A3 was expressed in low interference color which indicates a low level of mineralization. In the case of the 3-week-old rat, the RLM micrograph in Fig. 5 (B3) clearly shows the trend of bone mineralization in specific directions within the distinct spaces surrounding osteocyte lacunae represented by white dotted lines, which was not visible in BSE micrographs in Fig. 5 (column 2). Furthermore, the STEM-in-SEM micrograph in Fig. 5B4 suggests that mineralization was progressed from the outer rim toward the inner osteocyte lacuna. Based on this result with the differences between BSE micrographs and STEM-in-SEM micrographs, we can confirm that our CLEM technique is capable of providing information that was not available in prior imaging techniques used for bone investigation (Shah et al. 2019).

Comparative EDS analysis

In order to investigate chemical variations on the bone matrices during the femoral bone development according to age, we have performed STEM-in-SEM EDS on ROIs marked as yellow boxes in Fig. 5 (column 4). By utilizing area EDS analysis to biological UTS specimens, we were able to collect EDS signals from the specific desired area of the sample, particularly with focus on the bone matrix, thus producing more reliable data compared to previous chemical analysis which was conducted on powdered bone samples (Kim et al. 2018).

Elements were compared through their counts which were extracted as integrated intensity of each element peak from all spectra. Figures 6 and 7 display the chemical analysis data from 1- to 16-week-old SD rats obtained via STEM-in-SEM EDS. First, the increase of inorganic phases implies the increase of bone mineral density, which is better expressed in the ratio between Ca and P peak counts and total counts (Ca, P, C, N, and O) according to age as shown in Fig. 6A. The proportion of Ca and P increases significantly between 1- and 3-week-old individuals, which means that postnatal bone development occurs rapidly within the first 3 weeks (Burr and Allen 2013). Although the increase of bone mineral density continues up to 12 weeks, it significantly slows down after 3 weeks, which also corroborates with previous studies reporting the notable increase of femoral bone

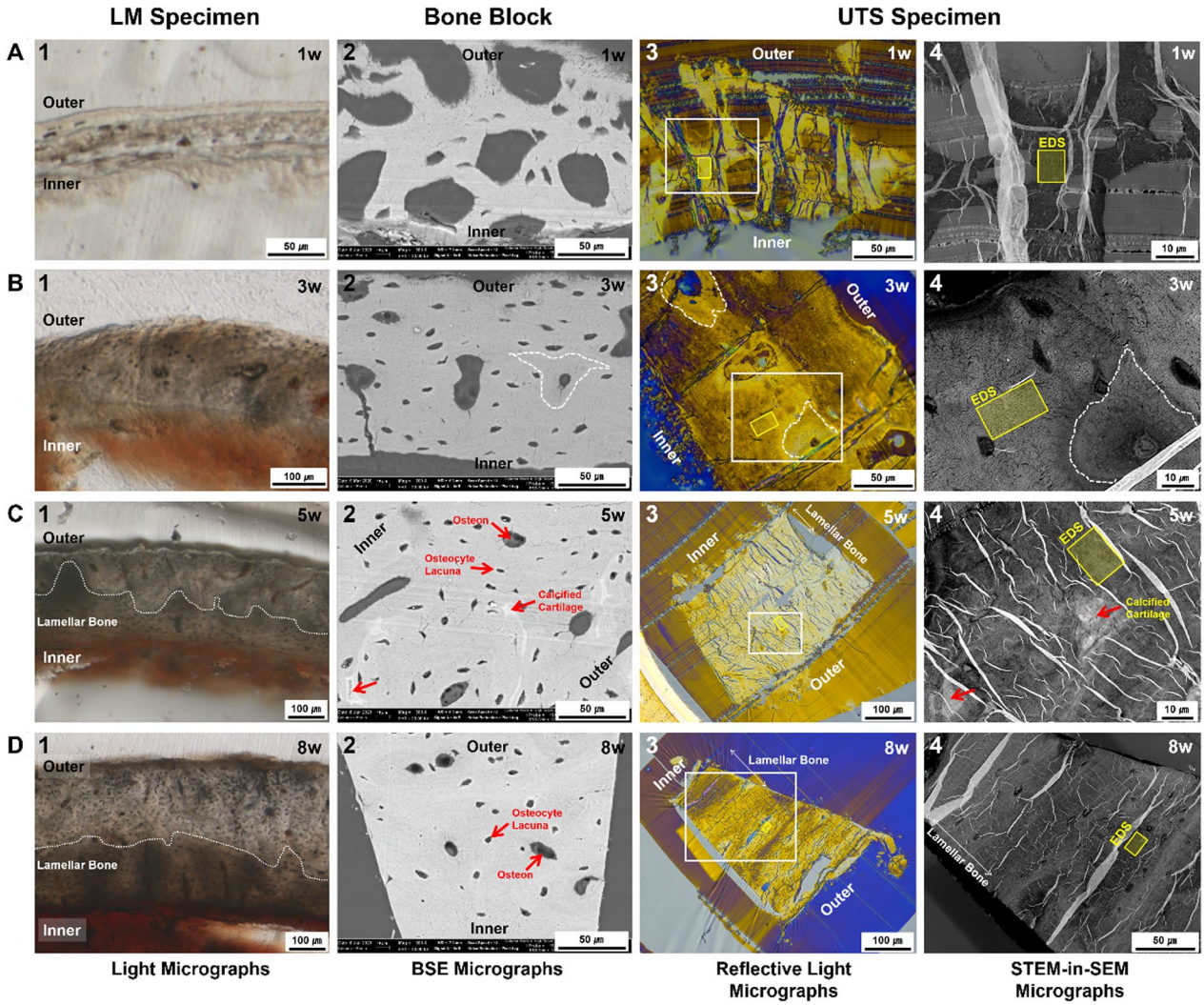

Fig. 5 Applied CLEM Micrographs of prepared specimens and bone blocks based on techniques introduced in Fig. 1. Rows **A**–**D** specify the age of the SD rats from 1- to 8-week-old individuals and columns (1 ~ 4) are arranged according to the type of microscopy technique used for CLEM. (BSE: Back-scattered electron. LM: Light microscopy. UTS: Ultra-thin sections)

mineral density of SD rats before 78 days, regardless of gender (Hansson et al. 1972; Fukuda and Iida 2004; Horton et al. 2008).

Figure 6C displays the correlation graphs plotting counts of the integrated intensity for the Ca and P peaks, which are the key elements constituting the inorganic phase. The Ca-P graph also includes data from the reference materials denoted as bold lines. The Ca-P graph shows that the slopes formed by data points do not deviate from the trend line of synthetic apatite, and the Ca/P ratio is relatively constant according to the ages of the rats within a certain range. These results agree with the previous studies which reported that the main mineral phase of bone is hydroxyapatite ($Ca_5(PO_4)_3(OH)$) (Wopenka and Pasteris 2005; Glimcher 2006; Wang et al. 2010). Figure 5D, the graph based on the calculated data from the slope shown in Fig. 6C provides a clearer representation of change in Ca/P according to advancing ages of the rats. In the case of the 1-week-old SD rat, the Ca/P distribution has a notably wide range, which indicates compositional inhomogeneity due to low mineralization during early stages of postnatal bone development. Moreover, we suggest that the high Ca/P ratio from the 1-week sample could have been affected by the higher cartilage proportion prior to extensive endochondral ossification (Burr and Allen 2013). In the case of the more mature rats, the Ca/P values are shown to have some variation without specific trends, but within a certain range (the mean values from ~ 1.44 to ~ 1.55). However, such Ca/P

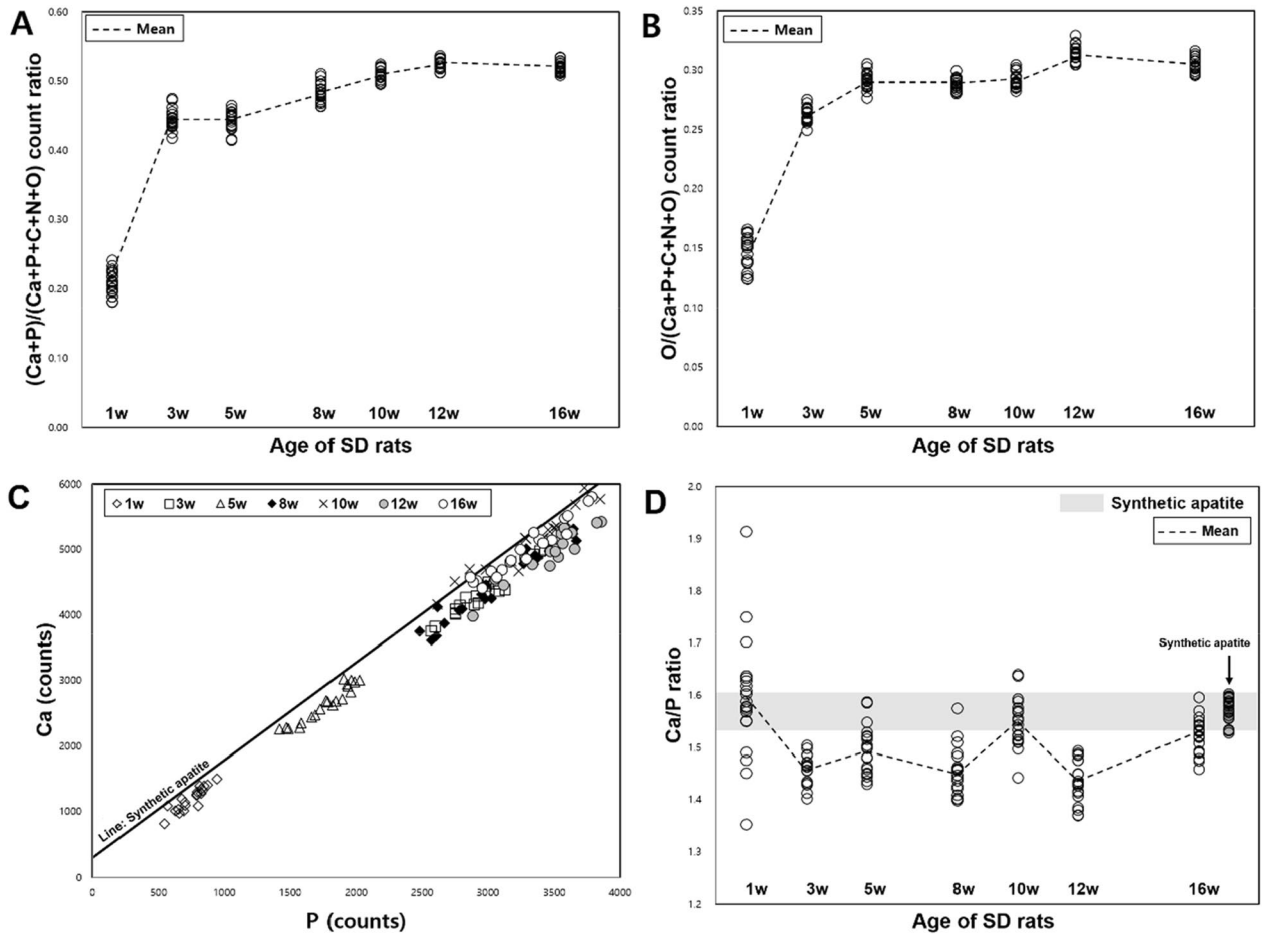

Fig. 6 Variations of inorganic elements among total bone constituents (Ca, P, C, N, and O) and comparative analysis of Ca and P content from 1- to 16-week-old SD rats acquired from 15 kV EDS data. **A** Variations of inorganic (Ca and P) elements among total bone constituents (Ca, P, C, N, and O). **B** Variations of oxygen originating from both organic and inorganic phases among total bone constituents (Ca, P, C, N, and O). **C** The counts correlation of Ca and P including reference material data expressed by the bold line. **D** Variations of Ca/P reconstructed from (C)

variations could occur due to differing nutrition and activity levels between individual rats (Masuyama et al. 2003; Friedman et al. 2015), and at a more fundamental level, the continuous ion substitution for bone mineral deposition by osteoblasts may result in slight variations in mineralization levels even between similarly aged rats (Fratzl et al. 2004; Hunt et al. 2008; Burr and Allen 2013).

In Fig. 6B, the trend of O proportion to the total counts was displayed to be similar with the trend of Ca and P in Fig. 6A, which suggests that most oxygen signals detected from the bone matrices originated from the inorganic phase. However, the O proportion in the 5-week-old rat has relatively high values compared to 3- and 8-week-old rats, respectively. In the case of oxygen, since its X-ray signals originates from both organic and inorganic phases, we have also considered variations of light elements (C and N) to interpret the subtle fluctuation of oxygen.

The trend of C and N counts among total counts (Ca, P, C, N, and O) representing the variation of organic phases is exactly the opposite to peak count ratio of Ca and P, and similar to the trend of C/O variations in Fig. 7D, further emphasizing the initial bone mineralization process and its continuation up to 12 weeks as previously mentioned.

In the case of C and O analysis, the characteristic X-rays of these lighter elements are more easily absorbed compared to Ca and P, which usually results in less reliable data. However, as UTS specimens have thin and even thickness, X-ray signals of C and O are less likely to be affected from the absorption effect and can be collected more stably (Williams and Carter 2009; Goldstein et al. 2018). In addition, we chose precipitated calcium carbonate as a reference material for C and O because

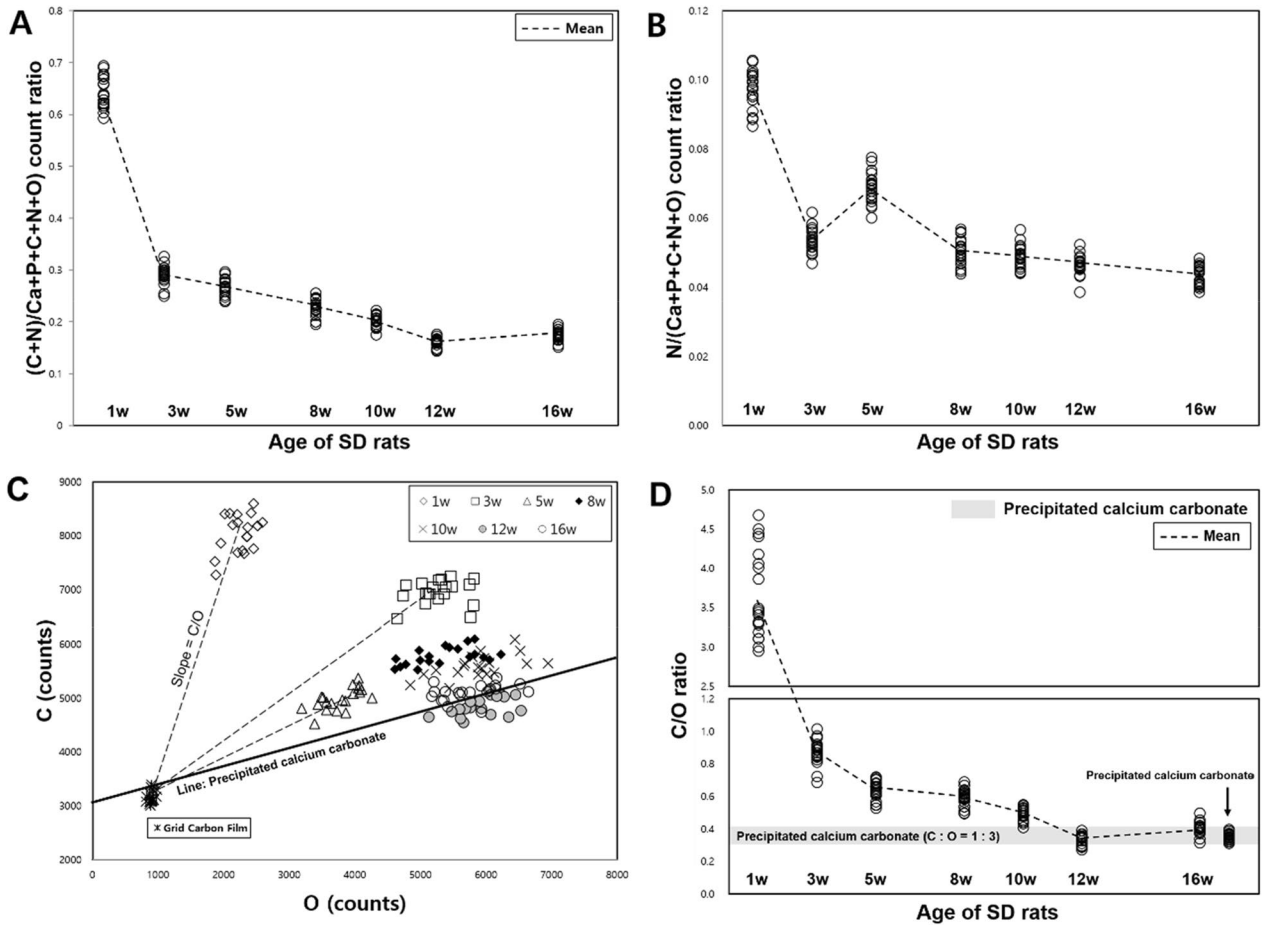

Fig. 7 Variations of organic elements among total bone constituents (Ca, P, C, N, and O) and comparative analysis of C and O content from 1- to 16-week-old SD rats acquired from 15 kV EDS data. **A** Variations of organic (C and N) elements among total bone constituents (Ca, P, C, N, and O). **B** Variations of nitrogen only from the organic phase among total bone constituents (Ca, P, C, N, and O). **C** The counts correlation of C and O including reference material data expressed by the bold line. **D** Variations of C/O reconstructed by slopes drawn from the grid film data in (C)

it was composed of nanoparticles small enough to minimize the absorption effect, and by utilizing the ultrasonic sprayer, the level of powder aggregation and dispersion was effectively controlled (Kim et al. 2018). Accordingly, the trend line data from precipitated calcium carbonate can be directly used for reference and comparative purposes with the data from SD rats (Fig. 7C). In order to mitigate potential issues related to C analysis, it is imperative to measure background C signals outside the samples because C signal sources may have diverse origins, especially within the EM analytical environment. We estimated the background C signal through analyzing the carbon film from the TEM grid. As the analytical conditions for all UTS samples were consistent and the analyses were performed in each single session, spectra from the carbon film also included the accumulated carbon contamination that occurs during EM analysis. As a result, as shown in the C–O graph (Fig. 7C), we presumed that the *y*-axis intercept of the precipitated calcium carbonate trend line represents the background signals from various sources. However, because the *y*-axis intercept of precipitated calcium carbonate only showed the background carbon but not oxygen, data from the TEM grid film were used as the datum point simultaneously representing carbon and oxygen, of which we used as a reference to recalculate the C proportion to O of SD rats. In Fig. 7C, the relative proportions of C to O were expressed as dashed lines having specific slopes which were drawn from the data of the TEM grid film to the data of each individual rat. In the case of the 1-week-old rat, the high slope represents high organic proportion during the early stages of bone development. The slopes from rats become lower with the increase in age, which indicates the relative decrease in proportion of organic phases as bone mineral density is increased at more advanced stages of bone development. By comparison with the slope of precipitated calcium carbonate, we can deduce that the atomic ratios of C to O from 12- and

16-week-old rats are close to CO_3. In Fig. 7D, the C/O ratio values were reconstructed by the slopes and calculated excluding the background carbon signal, in which the decrease of the C/O ratio generally indicates the decrease of organic phases and the increase of inorganic phases, since O is involved in both organic and inorganic phases. Based on the mean values of C/O, we observed a rapid decrease from the 1-week (~3.60) to 3-week (~0.91) old individuals, and much slower decreases from the 3-week to 12-week (~0.33) old individuals, approaching to the atomic C/O ratio of precipitated calcium carbonate (1/3), which is similar to the general bone composition ratio (Burr and Allen 2013).

In the case of carbon and oxygen, especially oxygen, it is difficult to effectively differentiate their exact placements, as these elements originate from both inorganic phases (such as bioapatite substituted by a small amount of CO_3) and organic phases (such as collagen, bone-forming proteins, and lipids) in bone (Figueiredo et al. 2012; Grunenwald et al. 2014; Mamede et al. 2018). Several studies reported the presence of the CO_3 group substituting the PO_4 or OH sites (Glimcher 2006; Wang et al. 2010; Burr and Allen 2013), and showed absorption bands of CO_3 in the inorganic phase utilizing Fourier transform infrared spectroscopy (FTIR), which also indicated that the amount of CO_3 is slightly increased according to age (Leventouri et al. 2009; Figueiredo et al. 2012; Grunenwald et al. 2014; Mamede et al. 2018). Nevertheless, our data presented in Figs. 8 and 9 do not indicate a distinguishable amount of inorganic carbon because of the predominant presence of organic carbon.

From a fundamental perspective of collagen composition, the atomic ratio of C: O is approximately 4:1 in type 1 collagen based on the Glycine-Proline-Hydroxyproline triplet unit (Fukuda and Iida 2004; Burr and Allen 2013). The C:O ratio of the 1-week-old individual in Fig. 7D is about 3.6:1, which is similar to that of collagen, which suggests that the oxygen proportion heavily depends on the carbon content of the organic phase. Therefore, organic oxygen should be rapidly reduced with carbon. Afterwards, the increase of oxygen is likely associated with the proliferation of inorganic phases during bone mineralization. As shown in Fig. 6A, although the mineralization level of 3- and 5-week-old individuals is very similar, the high O proportion of the 5-week individual shown in Fig. 6B is a peculiar feature compared to other rats. To discern factors that may cause such outliers, a deeper understanding of the remodeling cycle of bone involved in resorption, reversal, and formation is necessary. In addition, complex remodeling processes in localized regions within the compacta of femoral bones should also be taken into account (Herrikson et al. 2009; Burr and Allen 2013). Although a clearer interpretation

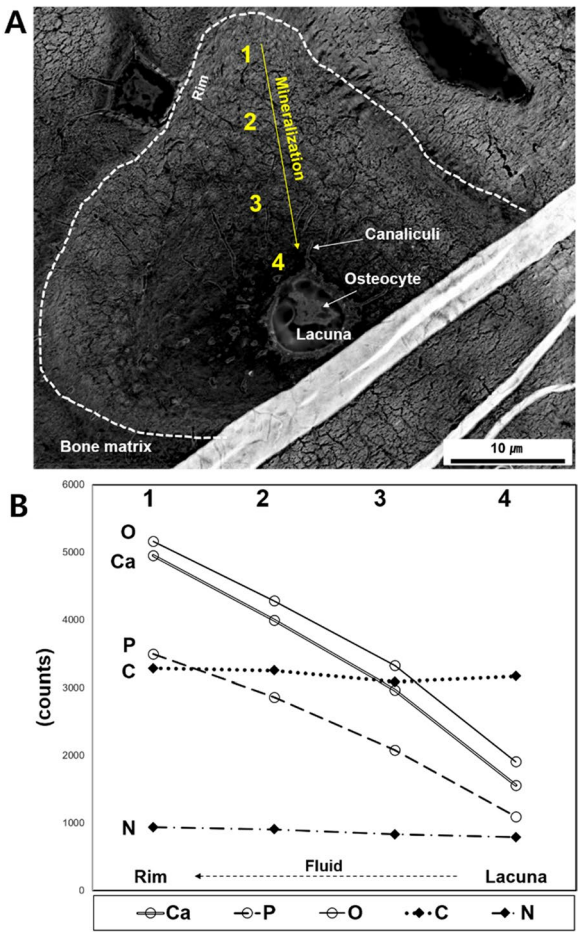

Fig. 8 Ossification of the area around the osteocyte lacuna from an 8-week-old rat. **A** STEM-in-SEM micrograph of the ROI from the 8-week-old rat in Fig. 5B4. **B** Count variations of each element (Ca, P, C, N, and O) from the outer rim toward the osteocyte lacuna. (ROI: Region of interest)

is required, light micrographs in Fig. 4 indicated that the femoral bone of the 5-week-old individual grew rapidly compared to the size of the 3-week-old individual, thus, opening the possibility of the enrichment of oxygen content related to the rapid developmental process. Additionally, as a result of Fig. 7B which gives us high nitrogen values in 5-week-old rat, it is presumed that enrich oxygen of 5-week-old rat was caused from organic action in the bone.

Based on other studies, poorly crystalline apatite crystals were suggested to be the major mineral component in vertebrates by FTIR spectrophotometry analysis (Cazalbou et al. 2004), and it has also been revealed that despite rapid mineralization since day 1, there is a notable lag of stiffening of the bone, and the stiffness level near adult bone was reached by 40 days of age (Miller et al. 2007). Therefore, we have also considered the possible presence of labile phases such as octacalcium phosphate which has

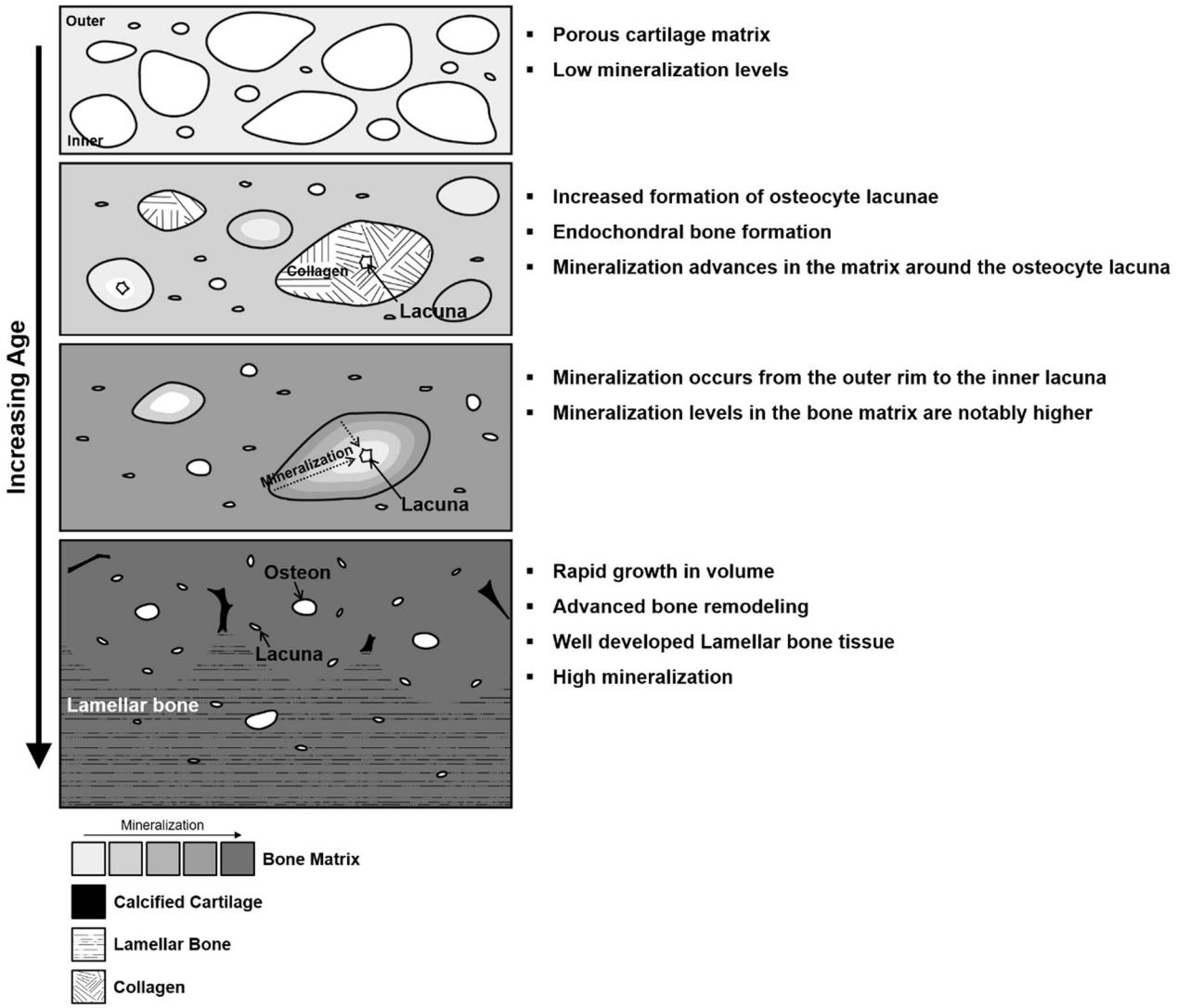

Fig. 9 Schematic diagram of the sequence of murine femoral bone development at an early stage. The bone matrix at an early stage has low mineralization levels and is highly porous. As mineralization progresses, the areas around the osteocyte lacunae are filled with collagen fibrils, and mineralization occurs from the outer rim toward the inner lacuna

a higher O proportion than that of hydroxyapatite, as one of the causation of high O proportion in the 5-week-old individual related to the rapid bone development in poor crystallization (Cazalbou et al. 2004; LeGeros et al. 2009).

Bone development in early stages

Variations of chemistry and microstructure for femoral bones from 1- to 16-week-old SD rats suggest that rapid volume growth and mineralization occur simultaneously within 8 weeks of age. In order to estimate the bone growth model at early stages, carrying out STEM-in-SEM EDS analysis provides us information on chemical variations of the ossification process around the osteocyte lacuna observed in a 3-week-old rat (Fig. 4B4). As a result, in Fig. 8, the graph presents the chemical variation of all elements (Ca, P, C, N, and O) around the osteocyte lacuna. The decrease of Ca, P, and O counts from the outer rim toward to inner osteocyte lacuna shows the mineralization progress direction. In addition, the constant C and N counts present the possibility that area around the osteocyte lacuna was filled with collagen prior to mineralization. In reported mechanisms of bone mineralization, through alkaline phosphatase, an ectoenzyme tethered to the osteoblast cell membrane cleaves inorganic pyrophosphate and generates inorganic phosphate, and inorganic ions participating in mineralization are controlled and localized to the collagen fibers (Murshed 2018). Our chemical data agrees with previous

studies, which can be discerned on the increase of inorganic ions toward the outer rim which is controlled by the osteocyte in the lacuna (Fukuda and Iida 2004; Xiong and O'Brien 2012; Burr and Allen 2013, Murshed 2018).

Based on the results by our CLEM techniques, the schematic diagram in Fig. 9 suggests the development sequence for femoral bone in the early stages of growth. The neonatal femoral bone is highly porous with very low levels of mineralization. The region around the osteocyte lacuna is mainly filled with collagen fibrils. Subsequently with advances in development, bone cells such as osteoblasts contributes to the role of mineralization to the surrounding area. We postulate that this mechanism may differ from the activation of cell groups responsible for forming secondary osteons (Haversian system) in more mature bones mentioned in previous studies (Harrison and Cooper 2015, Piemontese et al. 2017). In addition, we consider that the pores were rapidly filled preferentially with collagen fibrils by endochondral bone formation, because the postnatal development of femoral bone in early stages is significant prior to remodeling in more mature bones which promotes enhanced femoral growth and strength (Piemontese et al. 2017, Barreto et al. 2020). In the earliest postnatal stage, osteocyte lacunae and osteons are not clearly distinguishable, and these structural features are not well pronounced until 3-weeks old. After 5 weeks of age, we were able to confirm the distribution of osteons as prominent features in femoral bone, and the presence of lamellar bone tissue formed on the inner portion of the femur, which indicates the occurrence of bone remodeling for enhanced growth and strength (Burr and Allen 2013, Piemontese et al. 2017).

Conclusions

In this study, we suggested improved CLEM techniques which includes imaging techniques through RLM and STEM-in-SEM with the newly developed CLEM holder and its application for investigating the chemistry and structure of femoral bone from multiple SD rats at different growth stages. The CLEM holder was specifically designed to load nine grids and reduce fault (noise) signals from the holder itself, and can be efficiently utilized in both RLM and EM without the need to exchange samples. For imaging UTS specimens from femoral bone, RLM and STEM-in-SEM imaging presents high contrast and high resolution micrographs that can be correlated to subsequent STEM-in-SEM EDS analysis. STEM-in-SEM micrographs showed more detailed bone microstructure such as the boundaries by bone remodeling and mineralization compared to BSE micrographs. Especially, in the case of the 3-week-old rat, there was an indication of porous bone matrices being filled with collagen fibrils and bioapatite. Chemical investigation of femoral bones from SD rats at different growth stages was carried out with two reference materials as controls. By obtaining background C and O signals from the grid film and using the trend line of C and O counts obtained from precipitated calcium carbonate, we were able to construct more reliable counts correlation graphs of C and O for all SD rats. The C/O values of the rats represented their characteristic bone growth processes, which displayed a rapid decrease of C/O from 1- to 3-week-old individuals and much slower decreases from 3- to 12-week individuals. Variations of bone mineral density according to growth were more clearly displayed in the ratio between Ca and P counts and total counts (Ca, P, C, and O), which also supported that postnatal bone development occurred rapidly within the first 3 weeks. For understanding neonatal bone development, we performed STEM-in-SEM EDS analysis focused on the pores in femoral bone of 1- to 3-week-old rats. The chemical variation of our results show that bioapatite is localized after the pores are filled with collagen fibrils rather than occurring simultaneously, and the mineralization progressively becomes more prominent from the outer rim toward the inner osteocyte lacuna. Based on our results, we were able to postulate and provide insight on the growth mechanism for neonatal femoral bone. Furthermore, we expect that the presented CLEM techniques in this work can be further applied for more thorough investigation on the fundamental properties of bone, and can also be applied to other biological samples/biomaterials.

Abbreviations

CLEM	Correlative light and electron microscopy
EDS	Energy-dispersive spectroscopy
EM	Electron microscopy
FE	Field-emission
LM	Light microscopy
ROIs	Regions of interest
RLM	Reflective light microscopy
SD rat	Sprague-Dawley rat
SEM	Scanning electron microscopy
STEM-in-SEM	Scanning transmission electron microscopy-in-scanning electron microscopy
TEM	Transmission electron microscopy
UTS	Ultra-thin-section

Acknowledgements

This study was supported by the Korea Basic Science Institute (Institutional Program: D300400).

Author contributions

Conceptualization and experimental design: YEK, JKK, JGK, YJK. Multi-grid-holder development: YEK, JGK, HG. Sample preparation: JKK, YEK, ARJ. SEM instrument operation and data analysis: YEK, HG. Overall data analysis: YEK, JKK, YJK. Results interpretation and discussion: YEK, JKK, YJK, HG, JGK. Writing of the manuscript: YEK, JKK, YJK with input from all authors.

Funding

This study was funded by the Korea Basic Science Institute (Institutional Program: D300400).

Availability of data and materials
Data sharing is not applicable to this article as no datasets were generated or analyzed during the current study.

Declarations

Competing interests
The authors declare that they have no competing interests.

Author details
[1]Center for Scientific Instrumentation, Korea Basic Science Institute, 169-148 Gwahak-ro, Yuseong-gu, Daejeon 34133, South Korea. [2]Center for Research Equipment, Korea Basic Science Institute, 162 Yeongudanji-ro, Ochang-eup, Cheongwon-gu, Cheongju-si, Chungcheongbuk-do 28119, South Korea. [3]Research Center for Materials Analysis, Korea Basic Science Institute, 169-148 Gwahak-ro, Yuseong-gu, Daejeon 34133, South Korea. [4]Present Address: Natural History Division, National Science Museum, 481 Daedeokdaero, Yuseong-gu, Daejeon 34143, South Korea.

Received: 12 January 2023 Accepted: 14 August 2023
Published: 4 September 2023

References

Barreto IS, Cann SL, Ahmed S, Sotiriou V, Turunen MJ, Johansson U, Rodriguez-Fernandez A, Grünewald TA, Liebi M, Nowlan NC, Isaksson H. Multiscale characterization of embryonic long bone mineralization in mice. Adv Sci. 2020;7:2002524. https://doi.org/10.1002/advs.202002524.

Beyer Y, Beanland R, Midgley PA. Low voltage STEM imaging of multi- 292 walled carbon nanotubes. Micron. 2012;43:428–34.

Burr DB, Allen MR. Basic and applied bone biology, 1st ed. Academic Press Publishers. 2013.

Cazalbou S, Combes C, Eichert D, Rey C, Glimcher MJ. Poorly crystalline apatites: evolution and maturation in vitro and in vivo. J Bone Miner Metab. 2004;22:310–7. https://doi.org/10.1007/s00774-004-0488-0.

Figueiredo MM, Gamelas JAF, Martins AG. Characterization of bone and bone based graft materials using FTIR spectroscopy, Ch 18, Infrared spectroscopy—Life and biomedical sciences. InTech. 2012. https://doi.org/10.5772/36379.

Fratzl P, Gupta HS, Paschalis EP, Roschger P. Structure and mechanical quality of the collagen–mineral nano-composite in bone. J Mater Chem. 2004;14:2155–2123.

Friedman MA, Bailey AM, Rondon MJ, McNerny EM, Sahar ND, Kohn DH. Calcium- and phosphorus-supplemented diet increases bone mass after short-term exercise and increases bone mass and structural strength after long-term exercise in adult mice. PLoS One. 2015;11(3):e0151995. https://doi.org/10.1371/journal.pone.0151995.

Fukuda S, Iida H. Age-related changes in bone mineral density. J Vet Med Sci. 2004;66:755–60.

Glimcher MJ. Bone: Nature of the calcium phosphate crystals and cellular, structural, and physical chemical mechanisms in their formation. Rev Mineral Geochem. 2006;64:223–82.

Goldstein JI, Newbury DE, Michael JR, Ritchie NWM, Scott JHJ, Joy DC. Scanning electron microcopy and X-ray microanalysis, 4th ed. Springer Science Publishers. 2018.

Grunenwald A, Keyser C, Sautereau AM, Crubezy E, Ludes B, Drouet C. Revisiting carbonate quantification in apatite (bio)minerals—a validated FTIR methodology. J Archaeol Sci. 2014;49:134–41. https://doi.org/10.1039/c8ra05660a.

Guise O, Strom C, Preschilla N. STEM-in-SEM method for morphology analysis of polymer systems. Polymer. 2011;52:1278–85.

Hansson LI, Menander-Sellman K, Stenstrom A, Thorngren K-G. Rate of normal longitudinal bone growth in the rat. Calc Tiss Res. 1972;10:238–51.

Harrison KD, Cooper DML. Modalities for visualization of cortical bone remodeling: the past, present, and future. Front Endocrinol. 2015;6:122. https://doi.org/10.3389/fendo.2015.00122.

Herrikson K, Neutzsky-Wulff AV, Bonewald LF, Karsdal MA. Local communication on and within bone controls bone remodeling. Bone. 2009;44:1026–33.

Hodoroaba V-D, Unger WES, Hard AS. Characterization of nanoparticles, 1st ed, Elsevier Publishers. 2019.

Holm J, Keller RR. Angularly-selective transmission imaging in a scanning electron microscope. Ultramicroscopy. 2016;167:43–56.

Hondow N, Harrington J, Brydson R, Brown A. STEM mode in the SEM for the analysis of cellular sections prepared by ultramicrotome sectioning. J Phys Conf. 2012. https://doi.org/10.1088/1742-6596/371/1/012021.

Horton JA, Bariteau JT, Loomis RM, Strauss JA, Damron AA. Ontogeny of skeletal maturation in the juvenile rat. Anat Rec. 2008;291:283–92. https://doi.org/10.1002/ar.20650.

Hughes JM. The many facets of apatite. Am Miner. 2015;100:1033–9. https://doi.org/10.2138/am-2015-5193.

Hunt JR, Hunt CD, Zito CA, Idso JP, Johnson LK. Calcium requirements of growing rats based on bone mass, structure, or biomechanical strength are similar. J Nutr. 2008;138:1462–8.

Kim J-K, Kwon Y-E, Lee S-G, Jeong J-M, Kim J-G, Kim Y-J. Comparative SEM and TEM analyses of apatite phases prepared by a multi-sample loading device. Mater Charact. 2018;135:1–7.

Kwon Y-E, Kim J-K, Kim Y-J, Kim J-G, Kim Y-J. Development of SEM and STEM-in-SEM grid-holders for EDS analysis and their applications to apatite phases. J Anal Sci Technol. 2019;10:27. https://doi.org/10.1186/s40543-019-0186-0.

Kwon YE. Effective correlative light and electron microscopy (CLEM) Techniques applied to bone research [dissertation]. Chungnam National University. 2020. p84.

LeGeros RZ, Ito A, Ishikawa K, Sakae T, LeGeros JP. Fundamentals of hydroxyapatite and related calcium phosphates, Ch. 2 in Advanced biomaterials: fundamentals, processing, and applications. Wiley-American Ceramic Society 2009;19–52.

Leventouri TH, Antonakos A, Kyriacou A, Venturelli R, Liarokapis E, Perdikatsis V. Crystal structure studies of human dental apatite as a function of age. Int J Biomaterials. 2009. https://doi.org/10.1155/2009/698547.

Mamede AP, Vassalo AR, Cunha E, Gonçalves D, Parker SF, Batista de Carvalho LAE, Marques MPM. Biomaterials from human bone–probing organic fraction removal by chemical and enzymatic methods. RSC Adv. 2018. https://doi.org/10.1039/c8ra05660a.

Masuyama R, Nakaya Y, Katsumata S, Kajita Y, Uehara M, Tanaka S, Sakai A, Kato S, Nakamura T, Suzuki K. Dietary calcium and phosphorus ratio regulates bone mineralization and turnover in vitamin d receptor knockout mice by affecting intestinal calcium and phosphorus absorption. J Bone Miner Res. 2003;18:1217–26.

Mendis BG. Electron Beam-Specimen Interactions and Simulation Methods in Microscopy, 1st ed. Royal Microscopical Society. 2018.

Miller LM, Little W, Schirmer A, Sheik F, Busa B, Judex S. Accretion of bone quantity and quality in the developing mouse skeleton. J Bone Miner Res. 2007;22:1037–45. https://doi.org/10.1359/JBMR.070402.

Murshed M. Mechanism of bone mineralization. Cold Spring Harb Perspect Med. 2018. https://doi.org/10.1101/cshperspect.a031229.

Piemontese M, Almeida M, Robling AG, Kim H-N, Xiong J, Thostenson JD, Weinstein RS, Manolagas SC, O'Brien CA, Jilka RL. Old age causes de novo intracortical bone remodeling and porosity in mice. JCI Insight. 2017. https://doi.org/10.1172/jci.insight.93771.

Probst C, Gauvin R, Drew RAL. Imaging of carbon nanotubes with tin-palladium particles using STEM detector in a FE-SEM. Micron. 2007;38:402–8.

Shah FA, Ruscsák K, Palmquist A. 50 years of scanning electron microscopy of bone - a comprehensive overview of the important discoveries made and insights gained into bone material properties in health, disease, and taphonomy. Bone Research. 2019;7:15. https://doi.org/10.1038/s41413-019-0053-z.

Takizawa T, Robinson JM. Correlative fluorescence and transmission electron microscopy in tissues, Ch. 3 in Correlative light and electron microscopy, 1st ed. Academic Press Publishers. 2012; 37–57.

Wang X-Y, Zuo Y, Huang D, Hou X-D, Li Y-B. Comparative study on inorganic composition and crystallographic properties of cortical and cancellous bone. Biomed Environ Sci. 2010;23:473–80. https://doi.org/10.1016/S0895-3988(11)60010-X.

Williams DB, Carter CB. Transmission electron microcopy, 2nd edition. Springer Science Publishers. 2009.

Wopenka B, Pasteris JD. A mineralogical perspective on the apatite in bone. Mater Sci Eng C. 2005;25:131–43. https://doi.org/10.1016/j.msec.2005.01.008.
Wu W, Liu Z, Lin C, Hua J, Zeng Y. Application of low voltage in quantitative analysis by energy dispersive spectrum (EDS). Mater Sci Forum. 2015;804:165–8.
Xiong J, O'Brien CA. Osteocyte RANKL: new insights into the control of bone remodeling. J Bone Miner Res. 2012;27: 499505.

Publisher's Note